ACS Catalysis

pubs.acs.org/acscatalysis Research Article

Precise Regulation of the Coordination Environment of Single Co(II) Sites in a Metal−Organic Framework for Boosting CO_2 Photoreduction

Jingxue Wang, Kang Sun, Denan Wang, Xinwei Niu, Zhongyuan Lin, Siyuan Wang, Weijie Yang, Jier Huang, and Hai-Long Jiang*

Cite This: *ACS Catal.* 2023, 13, 8760−8769 Read Online

ACCESS | Metrics & More | Article Recommendations | Supporting Information

ABSTRACT: While the coordination environment around catalytic metal sites plays a crucial role in catalysis, its precise design and modulation still remain a challenge. Herein, the coordinated N atom number around single Co sites installed on a UiO-type metal−organic framework has been modulated to afford UiO-Co-N_x (x = 2, 3, and 4) for photocatalytic CO_2 reduction. Significantly, the photocatalytic performance is affected by the coordinated N atom number around the Co site, in which UiO-Co-N_3 exhibits superior activity to the other counterparts. Photo-/electrochemical results support the fastest charge transfer kinetics between the photosensitizer and UiO-Co-N_3. Theoretical calculations, together with the results acquired from in situ diffuse reflectance infrared Fourier transform spectra, manifest the lowest energy barriers of the rate-determining step and desorption energy of CO* over UiO-Co-N_3 among all UiO-Co-N_x samples.

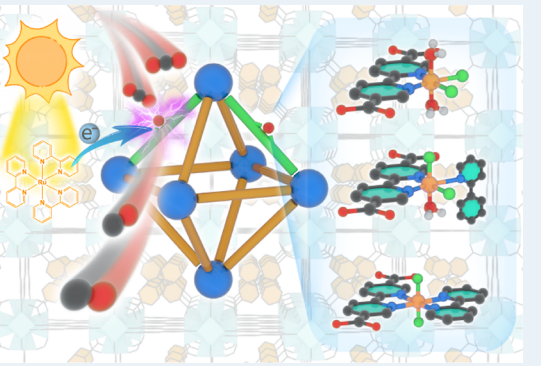

KEYWORDS: *metal−organic framework, single sites, CO_2 photoreduction, coordination environment, precise regulation*

Downloaded via UNIV SCIENCE AND TECHNOLOGY CHINA on July 14, 2023 at 02:26:54 (UTC).
See https://pubs.acs.org/sharingguidelines for options on how to legitimately share published articles.

1. INTRODUCTION

The growing global warming and energy supply issues have aroused the concern of the whole society; control of the concentration and reduction of CO_2 in the atmosphere should be put on the agenda.[1] Conversion of CO_2 to valuable chemical fuels is one of the most ideal approaches to achieve its resource utilization, in which CO_2 reduction by harnessing solar energy is regarded as a promising solution.[2−5] However, the efficiency of photocatalytic CO_2 reduction is far from satisfactory due to the very stable C═O bond and weak CO_2 adsorption on the common catalyst sites. To meet these challenges, the development of efficient photocatalysts for CO_2 reduction remains an urgent task.

In photocatalytic CO_2 reduction, the activity and selectivity are strongly dependent on the catalytic sites where the stable C═O bonds of CO_2 are broken and the activated CO_2 molecules are converted into chemical fuels.[2−4] The coordinated atoms around the catalytic sites are the most direct and prominent factors affecting the properties of catalytic centers.[6] In consequence, the coordination environment of catalytic sites could be a vital candidate for optimized CO_2 photoreduction performance.[7] Transition-metal M-N_x active centers are one of the most classical active sites in photocatalytic CO_2 reduction, and the coordination environment of the central metal site, such as the N atom number, N atom type, and other hetero-atoms, poses a significant impact on catalytic results.[7−11] Unfortunately, it is a challenge to rationally regulate the coordination environment around catalytic metal sites on the atomic level in conventional heterogeneous catalysts.[11−17] To our knowledge, systematic and precise regulation of the coordination environment in M-N_x sites with the exact number of N atoms has not yet been achieved in heterogeneous photocatalysts.

Metal−organic frameworks (MOFs), a class of crystalline porous materials assembled by metal ions/clusters with organic ligands,[18−23] possess well-defined and tailorable structures, which provide an ideal platform for structural design and accurate modification on the atomic level, bridging the heterogeneous and homogeneous catalysts.[24−28] In recent years, MOFs have been recognized to be very promising in CO_2 photoreduction.[29−36] Typically, different functional groups with chelating ability can be handily grafted onto MOF pore walls via mixed-ligand or post-synthetic modulation (PSM) strategies.[37−40] These chelating sites can immobilize different metal centers and allow further modification.[41−44]

Received: March 4, 2023
Revised: June 4, 2023
Published: June 16, 2023

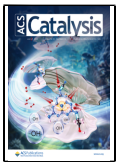

© 2023 American Chemical Society

https://doi.org/10.1021/acscatal.3c01003
ACS Catal. 2023, 13, 8760−8769

With the above thoughts in mind, MOFs might be the perfect candidates to precisely regulate the coordination environment around the catalytic metal sites for excellent performance in photocatalytic CO_2 reduction.

Herein, a UiO-type MOF bearing a bipyridine linker, UiO-67-20% bpy, has been deliberately synthesized to further install single Co(II) sites for photocatalytic CO_2 reduction. All three single-site Co(II) catalysts with different N coordination numbers are denoted as UiO-Co-N_x (x = 2, 3, and 4; x representing the number of pyridine N atoms coordinated with the Co center) (Scheme 1). The coordination environment around Co(II) sites has been confirmed by X-ray absorption spectroscopy (XAS). In photocatalytic CO_2 reduction, UiO-Co-N_x show distinct CO production activity with altered numbers of pyridine N atoms, and UiO-Co-N_3 exhibits the optimized performance. Systematic characterizations and theoretical calculations demonstrate that the coordinated N number not only regulates the charge-transfer dynamics but also affects the electronic density of single Co(II) sites, giving rise to different activation barriers of the key intermediates in CO_2 reduction. This work demonstrates that the unique advantages of MOFs make them an ideal platform to precisely design and modulate the coordination microenvironment of catalytic metal sites for excellent performance in photocatalytic CO_2 reduction.

Scheme 1. Illustration of the Stepwise Synthetic Strategies for UiO-Co-N_x (x = 2, 3, and 4) Catalysts

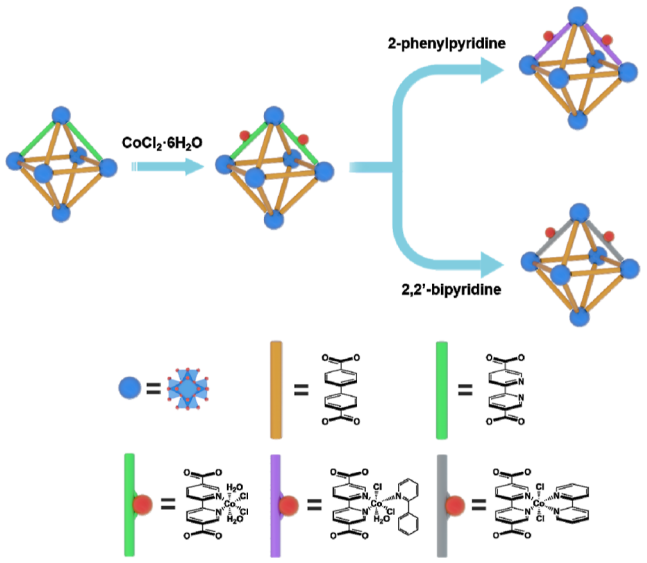

2. RESULTS AND DISCUSSION

The UiO-67-20% bpy was synthesized via a mixed-ligand strategy according to the previous report with some modifications.[45] The ^1H NMR confirms that the linkers contain 20% H_2bpydc (2,2-bipyridine-5,5-dicarboxylic acid) and 80% H_2bpdc (biphenyl-4,4′-dicarboxylic acid) (Figure S1 in the Supporting Information). The UiO-Co-N_2 was synthesized by stirring a mixed solution of UiO-67-20% bpy and $CoCl_2·6H_2O$. Then, UiO-Co-N_3 and UiO-Co-N_4 were constructed by further modifying UiO-Co-N_2 with 2-phenylpyridine (ppy) and 2,2′-bipyridine (bpy), respectively, where the Co loading of all samples remains ~1.0 wt % based on inductively coupled plasma atomic emission spectroscopy (ICP-AES) results (Table S1). Powder X-ray diffraction (PXRD) patterns of all samples are consistent with that of UiO-67, suggesting that the installation of Co(II) complexes with different coordination environments does not affect the crystallinity (Figure S2). Scanning electron microscopy (SEM) and transmission electron microscopy (TEM) observations

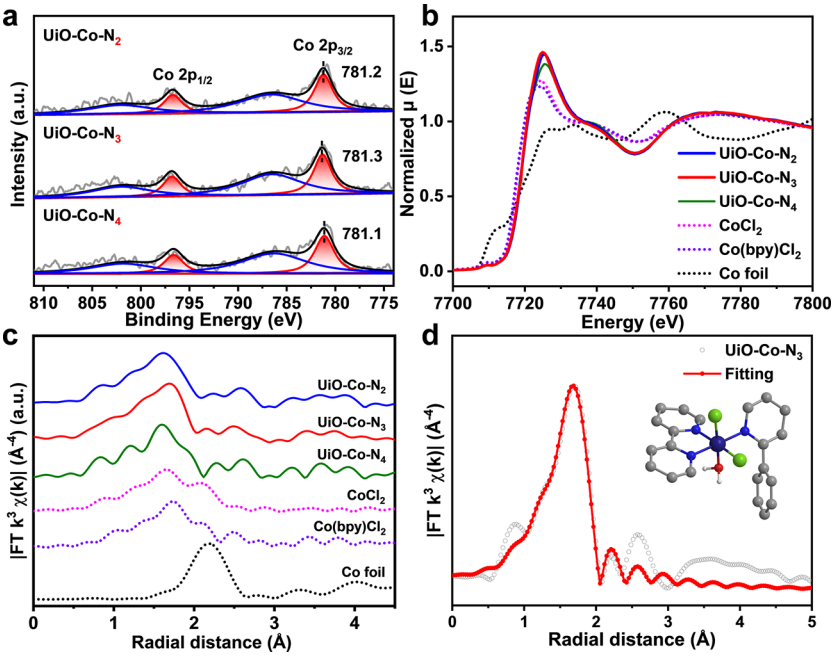

Figure 1. (a) XPS spectra for the Co 2p of UiO-Co-N_2, UiO-Co-N_3, and UiO-Co-N_4; (b) Co K-edge XANES spectra and (c) FT-EXAFS spectra of UiO-Co-N_2, UiO-Co-N_3, and UiO-Co-N_4 (solid lines), as well as Co^{II} and Co^0 reference compounds (dotted lines); and (d) EXAFS fitting of UiO-Co-N_3 (inset: proposed structure of the Co(II) sites coordinated by 2-phenylpyridine). The hydrogen atoms are omitted for clarity except for H_2O (C, gray; H, white; O, red; Cl, green; N, blue; and Co, navy blue).

https://doi.org/10.1021/acscatal.3c01003
ACS Catal. 2023, 13, 8760−8769

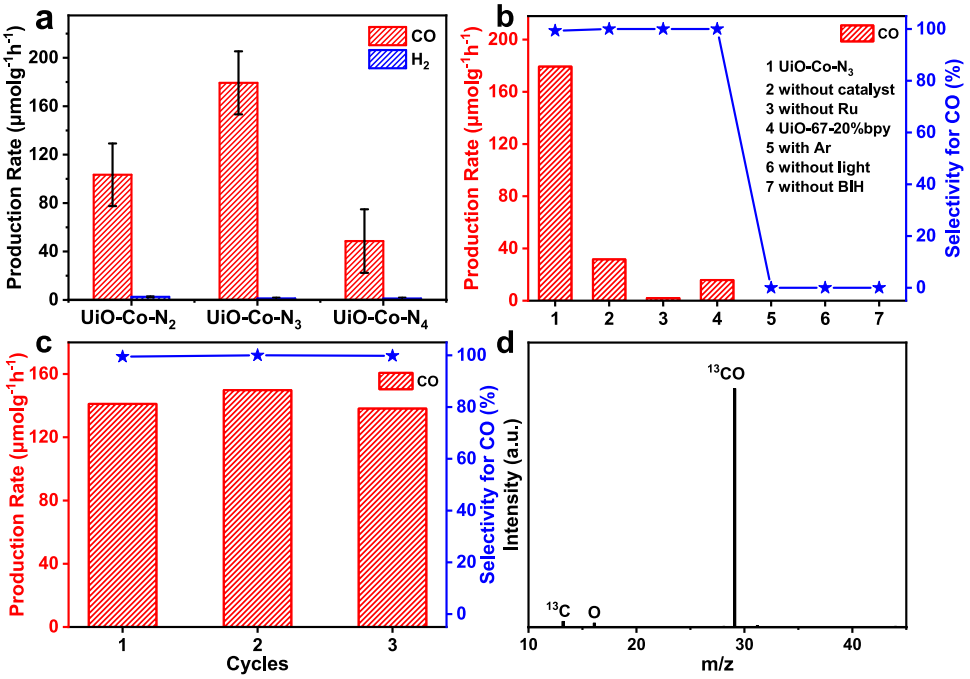

Figure 2. (a) Production rate of different catalysts for photocatalytic CO_2 reduction (the error bars represent the relative deviation obtained from three parallel experiments), reaction conditions: catalyst (10 mg), MeCN (20 mL), $Ru(bpy)_3Cl_2$ (30 mg), BIH (0.025 M), 300 W Xe lamp, $\lambda \geq 420$ nm; (b) photocatalytic CO_2 reduction performance under various reaction conditions; (c) recycling performance of UiO-Co-N_3 (the irradiation of each cycle lasts 2 h); and (d) mass spectrum for photocatalytic $^{13}CO_2$ reduction to ^{13}CO over UiO-Co-N_3.

indicate that these samples inherit the morphology and size of the parent UiO-67-20% bpy well; no apparent Co nanoparticles are observable in UiO-Co-N_x (x = 2, 3, and 4) (Figures S3−S6). Nitrogen sorption isotherms suggest very similar porous features after introducing the Co(II) complexes (Figure S7).

The specific coordination environments of Co(II) sites in UiO-Co-N_x were investigated. X-ray photoelectron spectroscopy (XPS) results indicate that the oxidation state of Co species is +2 in all samples,[46] and the binding energy of Co $2p_{3/2}$ follows the trend of UiO-Co-N_3 > UiO-Co-N_2 > UiO-Co-N_4 (Figure 1a), suggesting that the Co(II) electronic density follows the sequence of UiO-Co-N_3 < UiO-Co-N_2 < UiO-Co-N_4. To further resolve the local coordination structure of the Co(II) center in UiO-Co-N_x, steady-state XAS was conducted. The X-ray absorption near-edge spectroscopy (XANES) for UiO-Co-N_x at the Co K-edge shows a very similar absorption edge to $CoCl_2{\cdot}6H_2O$, indicating that the coordination structures in the three samples are likely in the octahedral geometry with a coordination number of six (Figure 1b).[38] In addition, the first-derivative XANES spectra present very similar edge positions to those of the $CoCl_2{\cdot}6H_2O$ and Co(bpy)Cl_2 references, suggesting that the oxidation state of the Co center in UiO-Co-N_x should be +2, which is in good accordance with the XPS results above (Figure S8). Moreover, Fourier transform-extended X-ray absorption fine structure (FT-EXAFS) spectra of UiO-Co-N_x show only one dominant peak at ∼1.62 Å, which originates from the Co−N bond or Co−O bond;[47,48] meanwhile, no peaks related to the Co−Co bond can be found, confirming that the single Co(II) sites are maintained during the post-synthetic modification (Figure 1c). The EXAFS fittings based on theoretical models are adopted to further gain details of the coordination configuration of Co(II) sites in UiO-Co-N_x. Specifically, the EXAFS fitting for UiO-Co-N_3 indicates that the distances of Co−N bonds with N atoms from bipyridine and 2-phenylpyridine are 2.05 and 2.14 Å, respectively, Co−Cl bond distance is 2.36 Å, and one H_2O molecule is coordinated with the Co(II) center with a distance of 2.09 Å (Figure 1d inset). Using similar fitting procedures, the coordination configurations of Co sites in UiO-Co-N_2 and UiO-Co-N_4 based on the EXAFS fittings and theoretical structural models are also performed, as shown in Figure S9, and the detailed fitting parameters are listed in Table S2. In addition, the ^{1}H NMR spectra further confirm that one Co site is coordinated with one N-containing ligand in UiO-Co-N_3 and UiO-Co-N_4 (Figures S10 and S11). Therefore, by modulating the Co(II) coordination environment with different numbers of N atoms, the Co(II) centers exhibit discriminative electronic density, which may give rise to differentiated performances in photocatalytic CO_2 reduction.

Inspired by the results above, photocatalytic CO_2 reduction experiments have been examined. UV−vis spectra manifest that there are some differences in light absorption, probably due to the different coordination environments of Co(II) sites (Figure S12). To eliminate this difference, a photosensitizer, $Ru(bpy)_3Cl_2{\cdot}6H_2O$ (abbreviated as [Ru-PS] hereafter, bpy = 2,2′-bipyridine), was added in the photocatalytic CO_2 reduction experiments. Gas chromatography indicates that only CO and H_2 can be observed in the gas-phase products, and no liquid products are detected by ion chromatography. After 2 h of light irradiation, the UiO-Co-N_2 catalyst without additional coordinated N atoms shows a CO evolution rate of 206.8 μmol/g with a turnover frequency (TOF) of 0.581 h^{-1} (Table S3). When one N atom is introduced, the CO production activity of UiO-Co-N_3 is significantly improved to 358.6 μmol/g with a TOF of 1.025 h^{-1}, which is 1.73 times higher than that of UiO-Co-N_2, and the selectivity of CO reaches 99.3%. The activity and selectivity are comparable to

https://doi.org/10.1021/acscatal.3c01003
ACS Catal. 2023, 13, 8760−8769

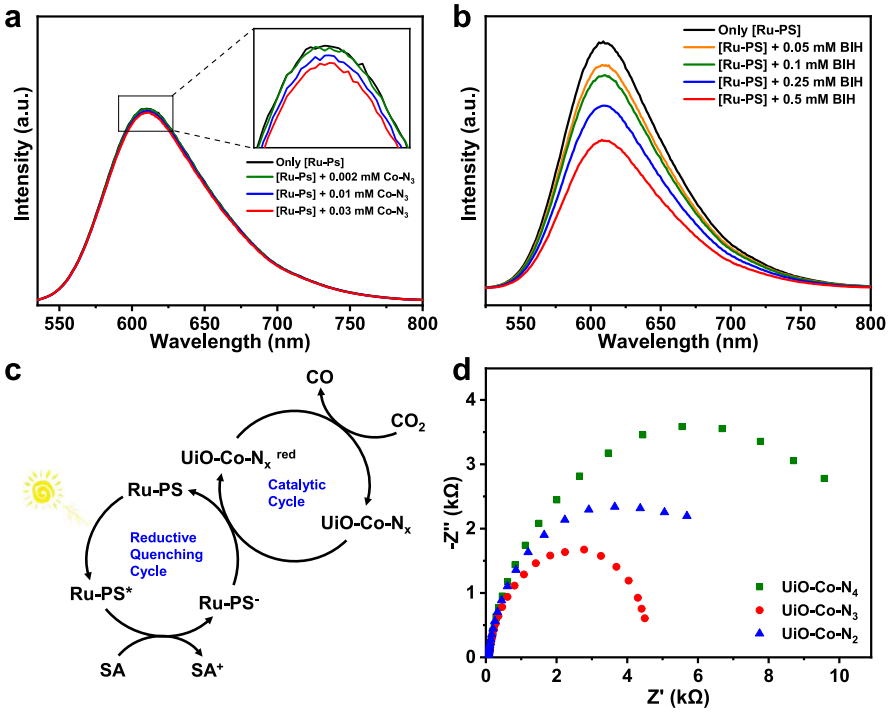

Figure 3. (a) Photoluminescence emission spectra (excited at 452 nm) of [Ru-PS] in MeCN containing different concentrations of Co(bpy)(ppy)Cl_2 (abbreviated as Co−N_3) molecules; (b) photoluminescence emission spectra (excited at 452 nm) of [Ru-PS] in MeCN containing different concentrations of BIH; (c) proposed catalytic cycles for UiO-Co-N_x with [Ru-PS] in MeCN; and (d) electrochemical impedance spectroscopy (EIS) plots of UiO-Co-N_2, UiO-Co-N_3, and UiO-Co-N_4 (EIS measurements were performed with a −1.32 V bias potential in the dark).

some recently reported MOF-based catalysts under similar conditions (Table S4). Unexpectedly, compared with the high activity of UiO-Co-N_3, the activity of UiO-Co-N_4 with coordination of more N atoms is only 97.2 μmol/g with a TOF of 0.278 h^{-1}, which is even much lower than that of UiO-Co-N_2 (Figure 2a). This result verifies that the difference of the coordinated N atom number around the Co(II) centers leads to distinctly different catalytic activities. As controls, an obviously reduced CO production rate is observed without catalysts. Moreover, trace amounts of CO are produced over UiO-67-20% bpy without Co(II) centers, suggesting that the chelating Co(II) sites are responsible for the catalytic process. Trace or no products can be found with Ar instead of CO_2 as the feeding gas or in the absence of light irradiation, [Ru-PS] or BIH, which demonstrates that the photosensitizer, sacrificial agent, CO_2, and light irradiation are all indispensable for CO_2 photoreduction (Figure 2b). Meanwhile, the single Co(II) sites installed onto the MOF show much enhanced activity compared to the corresponding homogeneous Co(II) counterparts, which manifests the significance of MOFs for improving the activity of molecular catalysts (Table S3). The stability of UiO-Co-N_3 was examined by recycling tests. Notably, the production rate and selectivity for CO remain unchanged after three consecutive cycles, and the PXRD patterns of UiO-Co-N_3 before and after photocatalytic reaction suggest that the crystallinity is well maintained, both of which support its good stability (Figures 2c and S13). Besides, there is no free 2-phenylpyridine in the reaction supernatant (Figures S14 and S15), and the Co content of UiO-Co-N_3 after the reaction was 0.96 wt %, which is close to that before the reaction (1.03 wt %), suggesting the stability of the skeleton of the catalyst. The source of CO was further identified via an isotopic experiment by only replacing $^{12}CO_2$ with $^{13}CO_2$ in the photocatalytic CO_2 reduction. As expected, the peak at m/z = 29 could be assigned to ^{13}CO, and no production of ^{12}CO (m/z = 28) is observed, unambiguously certifying that the carbon source of CO comes from CO_2 (Figure 2d).

To elucidate the mechanism of the differential CO_2 photoreduction performances caused by the altered numbers of coordinated N atoms around Co(II) sites, CO_2 absorption, charge transfer from [Ru-PS] to UiO-Co-N_x, and the CO_2 reduction processes have been carefully investigated. The adsorption of CO_2 molecules on the catalyst is the first step.[29] However, the three catalysts exhibit similar adsorption capacities to the parent UiO-67-20%bpy, illustrating that the post-synthetic modification does not affect CO_2 adsorption, from which it is assumed that the differences in the photocatalytic performance do not originate from the different CO_2 adsorption capacities (Figure S16). Therefore, photoelectrochemical measurements have been implemented to investigate the charge transfer kinetics. When [Ru-PS] acts as a photosensitizer in photocatalysis, there are usually two charge quenching paths including oxidative quenching and reductive quenching.[49] The charge transfer and quenching paths have been studied through photoluminescence (PL) experiments, where the homogeneous Co(bpy)(ppy)Cl_2 (abbreviated as Co−N_3) was adopted to assess the quenching process. The PL spectra suggest that the quenching rate constant (k_q) of Co−N_3 is 7.3 × 10^8 M^{-1} s^{-1}, which is lower than that of BIH with a k_q of 1.2 × 10^9 M^{-1} s^{-1} (Figure S17), supporting a reductive quenching in the photocatalytic process (Figure 3a,b). Then, the band structures of UiO-Co-N_x are evaluated by Tauc and Mott−Schottky plots, suggesting that the conduction band minimum (CBM) positions of UiO-Co-N_2, UiO-Co-N_3, and

https://doi.org/10.1021/acscatal.3c01003
ACS Catal. 2023, 13, 8760−8769

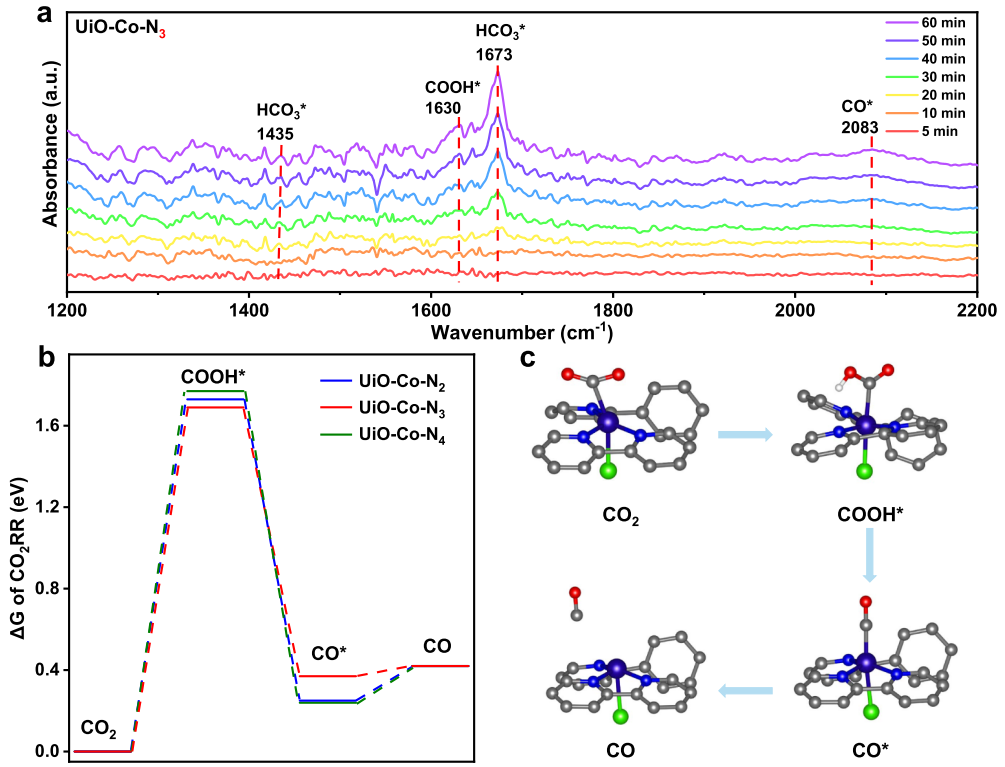

Figure 4. (a) In situ DRIFTS spectrum for detecting the reaction intermediates in CO_2 photoreduction over UiO-Co-N_3 under visible light irradiation; (b) free energy diagram describing the process of CO_2 reduction to CO via the COOH* intermediate over UiO-Co-N_2, UiO-Co-N_3, and UiO-Co-N_4 under visible light irradiation; and (c) structure models of the reaction path in photocatalytic CO_2 reduction by UiO-Co-N_3. The hydrogen atoms are omitted for clarity except for COOH* (C, gray; H, white; O, red; Cl, green; N, blue; and Co, navy blue).

UiO-Co-N_4 are −1.27, −1.02, and −1.18 V vs SCE, respectively (Figures S18−S20). The reductive electron-transfer quenching potential of [Ru-PS]/[Ru-PS]$^-$ (−1.33 V vs SCE) is more negative than the CBM positions of UiO-Co-N_x,[49−51] illustrating that it is thermodynamically feasible for electron transfer from [Ru-PS]$^-$ to UiO-Co-N_x. Therefore, based on the results above, the mechanism of CO_2 photoreduction can be proposed. Under light irradiation, the photosensitizers are excited, followed by a fast reductive quenching that electron transfer from BIH to the excited [Ru-PS]*, generating [Ru-PS]$^-$ that could donate the electron to generate [UiO-Co-N_x]^{red}.[40] Subsequently, the CO_2 is reduced by [UiO-Co-N_x]^{red} and [Ru-PS]$^-$ is back to the ground state, achieving a catalytic cycle (Figure 3c). In the PL emission spectra of [Ru-PS] with different catalysts, the fluorescence intensity of [Ru-PS] in the presence of UiO-67-20% bpy is nearly unchanged, while obvious PL quenching occurs after introducing Co counterparts, and the quenching degree follows the order UiO-Co-N_3 > UiO-Co-N_2 > UiO-Co-N_4 (Figure S21), which proves a faster charge transfer between [Ru-PS] and UiO-Co-N_3 and accordingly the superior photocatalytic performance of UiO-Co-N_3. In addition, cyclic voltammetry (CV) of all catalysts indicates that the Co sites present different reduction potentials from Co(II) to Co(I), probably suggesting that Co sites in UiO-Co-N_3 are more easily reduced in catalysis (Figure S22). Therefore, the faster charge transfer in UiO-Co-N_3 is probably due to the lower electron density of the Co(II) sites, making it easier to accept electrons from the excited [Ru-PS], which is also supported by XPS results (Figure 1a). Furthermore, the electrochemical impedance spectroscopy (EIS) plots of UiO-Co-N_x manifest that the radius of the Nyquist plots follows the trend of UiO-Co-N_4 > UiO-Co-N_2 > UiO-Co-N_3, revealing the lower resistance for interfacial charge transfer in UiO-Co-N_3 (Figure 3d). The above results unambiguously demonstrate that the different coordination environments, i.e., altered numbers of N atoms, can modulate the electronic structure of catalytic Co(II) sites, leading to faster charge transfer kinetics for enhanced performance in photocatalytic CO_2 reduction.

To gain in-depth insights into the CO_2 reduction process, in situ diffuse reflectance infrared Fourier transform spectroscopy (DRIFTS) and density functional theory (DFT) calculations were performed to identify the intermediates in CO_2 photoreduction.[32] In DRIFTS, the obvious peaks at 1435 and 1673 cm^{-1} are related to HCO_3* species, which may be generated from the chemisorption of CO_2 on the catalyst surface.[30,52] After light irradiation, the gradually increasing peak at 1630 cm^{-1} is attributed to COOH*, which is the key intermediate in the conversion of CO_2 to CO. The observed CO* signal at 2083 cm^{-1} supports the production of CO (Figure 4a).[40] Hence, the proposed pathway of photocatalytic CO_2 reduction is speculated as follows

$$^* + CO_2 \rightarrow CO_2^* \quad (1)$$

$$CO_2^* + H^+ + e^- \rightarrow COOH^* \quad (2)$$

$$COOH^* + H^+ + e^- \rightarrow CO^* + H_2O \quad (3)$$

$$CO^* \rightarrow CO\uparrow + ^* \quad (4)$$

Furthermore, DFT calculations were employed to figure out the CO_2 activation process. Based on the mechanism of CO_2 reduction gained by DRIFTS, the reaction undergoes CO_2

https://doi.org/10.1021/acscatal.3c01003
ACS Catal. 2023, 13, 8760−8769

molecule binding to the Co sites, proton-coupled electron transfer (PCET) of adsorbed CO_2* molecules, and desorption of CO* to CO (Figures 4b,c and S23 and S24). First, the desorption energy of H_2O molecules is much lower than that of Cl over UiO-Co-N_2 and UiO-Co-N_3 (Table S5), indicating that the Co sites in UiO-Co-N_2 and UiO-Co-N_3 accept electrons and remove H_2O molecules to bind CO_2 molecules, while the Co sites in UiO-Co-N_4 have to desorb one Cl to adsorb CO_2. Second, in the PCET process, the rate-determining step in the overall photocatalytic CO_2 reduction is the generation of the crucial intermediate COOH*. As expected, UiO-Co-N_3 exhibits the lowest energy barrier among all UiO-Co-N_x, indicating that the single Co sites coordinated with three N atoms is more favorable for CO_2 reduction (Figure 4b and Table S6). Finally, the desorption of CO* from the Co centers can proceed with the desorption energy of CO* of 0.17, 0.05, and 0.18 eV for UiO-Co-N_2, UiO-Co-N_3, and UiO-Co-N_4, respectively, showing that CO* is more preferable to detach from the Co sites in UiO-Co-N_3. Overall, the lowest energy barriers of both COOH* production and CO* desorption over UiO-Co-N_3 account for the highest CO_2 photoreduction activity.

3. CONCLUSIONS

To sum up, we have successfully achieved precise regulation of the coordination environment, i.e., altered numbers of coordination N atoms around catalytic Co(II) sites in MOFs by a simple PSM strategy. The different numbers of pyridine N atoms coordinated to the Co(II) sites in UiO-Co-N_x (x = 2, 3, and 4) are unambiguously confirmed by XAS. Among them, UiO-Co-N_3 displays a superior CO_2 photoreduction activity to UiO-Co-N_2 and UiO-Co-N_4, demonstrating the important influence of the coordination environment around catalytic centers on catalysis. Systematic experiments and theoretical calculations indicate that the best photocatalytic performance of UiO-Co-N_3 originates from the faster charge transfer kinetics between [Ru-PS] and UiO-Co-N_3, as well as the optimized energy paths in the CO_2 photoreduction process. This work develops a facile strategy for precise modulation of the coordination environment around catalytic metal sites and highlights the significant relationship between the coordination microenvironment and catalysis.

4. EXPERIMENTAL SECTION

4.1. Materials and Instrumentation. All chemicals were purchased commercially without further treatment unless stated otherwise: *N*,*N*-dimethylformamide (DMF, Sinopharm Chemical Reagent Co., Ltd., AR), zirconium chloride ($ZrCl_4$, Aladdin Industrial Inc., 99.9%), 2,2-bipyridine-5,5-dicarboxylic acid (H_2bpydc, Energy Chemical, 98%), 4,4′-diphenyldicarboxylic acid (H_2bpdc, Energy Chemical, 98%), glacial acetic acid (CH_3COOH, Sinopharm Chemical Reagent Co., Ltd., AR), cobalt(II) chloride hexahydrate ($CoCl_2{\cdot}6H_2O$, Sinopharm Chemical Reagent Co., Ltd., AR), $Ru(bpy)_3Cl_2{\cdot}6H_2O$ (Energy Chemical, 98%), iodomethane (CH_3I, Energy Chemical, 99.5%), 2-phenylbenzimidazole (Energy Chemical, 98%), methanol (MeOH, Sinopharm Chemical Reagent Co., Ltd., AR), ethanol (EtOH, Sinopharm Chemical Reagent Co., Ltd., AR), 2-phenylpyridine (ppy, Macklin, 98%), 2,2′-bipyridine (bpy, Macklin, 99%), acetonitrile (MeCN, Sinopharm Chemical Reagent Co., Ltd., AR), sodium sulfate (Na_2SO_4, Sinopharm Chemical Reagent Co., Ltd., AR), tetrabutylammonium hexafluorophosphate (Aladdin Industrial Inc., 98%), mesitylene (Energy Chemical, 98%), dimethyl sulfoxide-d_6 (DMSO-d_6, Energy Chemical, 99.8%), and hydrofluoric acid (HF, Macklin, 40%). Deionized water (18.25 MΩ·cm) was acquired by reversed osmosis followed by ion exchange and filtration (Cleaned Water Treatment Co., Ltd., Hefei).

PXRD patterns were measured on a Japan Rigaku MiniFlex 600 equipped with graphite monochromatized Cu Kα radiation (λ = 1.54178 Å). ^{1}H nuclear magnetic resonance (^{1}H NMR, Bruker AVANCE AV III 400) spectroscopy was used to confirm the proportion of mixed ligands and the amounts of nitrogen ligands in the obtained MOF by HF with DMSO-d_6. SEM images were obtained on a Carl Zeiss Supra 40 scanning electron microscope. TEM images were taken on a JEOL JEM-2100F field-emission transmission electron microscope. Gas sorption measurements were conducted by using automatic volumetric adsorption equipment (Micromeritics ASAP 2020). Prior to the measurements, the samples were immersed in acetone for 24 h and then activated in vacuum at 100 °C. The contents of Co species in the catalysts were determined by an Optima 7300 DV inductively coupled plasma atomic emission spectrometer. UV−vis diffuse reflectance data were recorded on a Shimadzu UV-2700 spectrophotometer, and a white standard of $BaSO_4$ was used as a reference. XPS measurements were conducted by using an ESCALAB 250 high-performance electron spectrometer with monochromatized Al Kα ($h\nu$ = 1486.7 eV) as the excitation source. PL measurements were collected on a Hitachi FL-4600 fluorescence spectrometer. The gaseous products of photocatalytic CO_2 reduction were analyzed and identified by gas chromatography (Shimadzu GC-2014). The liquid products were analyzed using ion chromatography (Thermo Scientific Dionex Aquion). Gas chromatography−mass spectrometry (GC−MS) was utilized to analyze the isotope-labeled products on an Agilent Technologies 7890B GC system equipped with an Agilent Technologies 5977B MSD mass spectrometer and an HP-MOLESIEVE (30 m × 0.32 mm × 25 μm) column. High-performance liquid chromatography (HPLC) was used to detect the mixture after the photoreaction on the Shimadzu Prominence LC-20A series HPLC system with the HPLC AD-H column (5% isopropanol in hexanes, 1.0 mL/min, λ = 208 nm).

4.2. Experimental Details. *4.2.1. Catalyst Synthesis. 4.2.1.1. Preparation of UiO-67-20%bpy.* UiO-67-20%bpy was synthesized according to the reported method with some modifications.[45] Typically, $ZrCl_4$ (96.0 mg, 0.41 mmol), biphenyl-4,4′-dicarboxylic acid (H_2bpdc, 79.1 mg, 0.33 mmol), and 2,2′-bipyridine-5,5′-dicarboxylic acid (H_2bpydc; 19.9 mg, 0.08 mmol) were dissolved in DMF (16 mL) with acetic acid (768 μL) in a glass vial (20 mL), followed by sonication for 5 min. Then, the glass vial was placed in an oven at 120 °C for 24 h. After cooling to room temperature, the solid was collected by centrifugation and washed 3 times with DMF and methanol, respectively. The obtained precipitates were dried at 70 °C to afford a white powder.

4.2.1.2. Preparation of UiO-Co-N_2. The UiO-Co-N_2 was obtained by stirring UiO-67-20%bpy (50.0 mg) with $CoCl_2{\cdot}6H_2O$ (2.5 mg, 0.01 mmol) in acetonitrile (10 mL) at 25 °C for 12 h and then washing 3 times with acetonitrile until the supernatant became colorless. The precipitates were dried at 60 °C under vacuum overnight.

https://doi.org/10.1021/acscatal.3c01003
ACS Catal. 2023, 13, 8760−8769

4.2.1.3. Preparation of UiO-Co-N_3. The UiO-Co-N_3 was obtained by stirring UiO-Co-N_2 (50.0 mg) with 2-phenylpyridine (1.5 mg, 0.01 mmol) in acetonitrile (20 mL) at 25 °C for 12 h and then washing with acetonitrile and drying at 60 °C under vacuum overnight.

4.2.1.4. Preparation of UiO-Co-N_4. The UiO-Co-N_4 was obtained by stirring UiO-Co-N_2 (50.0 mg) with 2,2′-bipyridine (1.5 mg, 0.01 mmol) in acetonitrile (20 mL) at 25 °C for 12 h and then washing with acetonitrile and drying at 60 °C under vacuum overnight.

4.2.1.5. Preparation of Co(bpy)Cl_2. The Co(bpy)Cl_2 was synthesized according to the reported method with some modifications.[53] Typically, $CoCl_2{\cdot}6H_2O$ (4.4 g, 18.5 mmol) and 2,2′-bipyridine (2.9 g, 18.5 mmol) were dissolved in ethanol (150 mL) in a round-bottom flask (250 mL). The resulting mixture was stirred for 1 h and then filtered and washed with ethanol several times. The precipitates were evaporated at room temperature, and a blue powder was obtained.

4.2.1.6. Preparation of Co(bpy)(ppy)Cl_2. The Co(bpy)(ppy)Cl_2 was obtained by stirring Co(bpy)Cl_2 (441 mg, 1.0 mmol) with 2-phenylpyridine (155 mg, 1.0 mmol) in acetonitrile (20 mL) at 25 °C for 12 h and then washing with acetonitrile. The precipitates were evaporated at room temperature.

4.2.1.7. Preparation of 1,3-Dimethyl-2-phenyl-2,3-dihydro-1H-benzo[d]imidazole (BIH). BIH was synthesized according to the reported method with some modifications.[54] Typically, 2-phenylbenzimidazole (1.5 g, 7.7 mmol) and methyl iodide (4.0 g, 28.2 mmol) were dissolved in methanol (7.5 g) containing NaOH (0.3 g, 0.008 mmol) in a pressure tube (15 mL). The mixture was heated overnight at 110 °C. Then, the obtained crude product was collected and decolorized by the activated carbon in the hot EtOH/H_2O (5:1 v/v) solvent, and the white precipitates were recrystallized from ethanol. The resulting product (3.0 g) was further dissolved in methanol (80 mL) in a round-bottom flask (250 mL) with the slow addition of $NaBH_4$ (1.2 g, 31.7 mmol). Then, the white mixture was stirred for 1 h under a N_2 atmosphere at 0 °C. After removing the solvent under reduced pressure, the white precipitates were recrystallized from the EtOH/H_2O (2:1 v/v) solvent to obtain the colorless crystalline product for further use in photocatalytic CO_2 reduction.

4.2.2. Photocatalytic CO_2 Reduction. Typically, the photocatalytic CO_2 reduction was performed in a 160 mL photoreactor (Beijing Perfect Light Technology Co., LTD, China). A mixture of the catalyst (10.0 mg), acetonitrile (MeCN, 20 mL), Ru(bpy)$_3Cl_2{\cdot}6H_2O$ (30.0 mg), and BIH (0.025 M) was added into the photoreactor with stirring at ambient temperature. After homogeneous mixing, the suspension was purged with pure CO_2 for 15 min to remove air. The photoreactor with the reacting solution was irradiated by the Xe lamp (LX-300F, Japan) equipped with a 420 nm filter ($\lambda \geq 420$ nm). For each evaluation of the products from CO_2 reduction, 200 μL of the headspace was chosen for injection into the gas chromatography (Shimadzu GC-2014, argon as a carrier gas) equipped with a thermal conductivity detector and a flame ionization detector and quantified by a calibration plot to the internal hydrogen and CO standards. The liquid product was detected by ion chromatography.

In the recycling experiments, the catalysts were collected by centrifugation after every 2 h of irradiation, washed 3 times with acetonitrile, and then redispersed in acetonitrile to be reused in the next run under the standard reaction conditions.

The isotope-labeled experiment was performed by only replacing $^{12}CO_2$ with $^{13}CO_2$, and the gas products were analyzed by gas chromatography−mass spectrometry (GC−MS).

After the photoreaction, the solution was obtained by centrifugation of the solid catalysts first and then purified by filtration membrane. After that, 1 mL of the solution was diluted by 9 mL of deionized water for the ion chromatography test.

4.2.3. X-ray Absorption Spectroscopy. XAS was measured at the beamline 12-BM at the Advanced Photon Source, Argonne National Laboratory. The XAS data were collected at room temperature with the fluorescence mode using a Vortex-ME7 solid-state detector. The powder samples were dispersed on Kapton tape during the measurements. The measurements were carried out using the apparatus described in previous reports.[55,56] The XANES and EXAFS data analyses were performed with the Athena and Artemis packages based on FEFF programs.

4.2.4. EIS, Mott−Schottky Plot Measurements, and CV Measurements. Electrochemical impedance spectra and Mott−Schottky plot measurements were collected on the Zahner Zennium electrochemical workstation in a standard three-electrode system, with catalyst-coated glassy carbon (Φ = 3 cm) as the working electrode, a Pt plate as the counter electrode, and Ag/AgCl as the reference electrode. Typically, 2.0 mg of catalysts was dispersed into the mixture of 10 μL of 5 wt % Nafion and 2 mL of ethanol, and 45 μL of the mixture was used to coat the glassy carbon (Φ = 3 cm). A 0.1 M Na_2SO_4 solution was used as the electrolyte. EIS measurements were performed with a −1.32 V bias potential in the dark. The frequencies of Mott−Schottky plot measurements are 500, 1000, and 1500 Hz.

CV measurements were conducted on a CHI 760E electrochemical workstation (Chenhua Instrument, Shanghai, China) in a standard three-electrode system at room temperature, with the catalyst-coated glassy carbon (Φ = 3 cm) as the working electrode, a Pt plate as the counter electrode, and Ag/Ag^+ as the reference electrode. Typically, 3.0 mg of catalysts was dispersed into the mixture of 10 μL of 5 wt % Nafion and 2 mL of ethanol, and 45 μL of the mixture was used to coat the glassy carbon. 0.1 M tetrabutylammonium hexafluorophosphate in acetonitrile solution was used as the electrolyte after deoxidation by N_2. The ferrocene was used as an internal standard, and the ferrocenium/ferrocene (Fc^+/Fc) potential (+0.40 V vs SCE in acetonitrile) was used to correct potentials vs SCE.[57,58] The measurements were performed under a scan rate of 200 mV/s under N_2.

4.2.5. PL Emission Spectra. The steady-state PL spectra were measured by a Hitachi FL-4600 fluorescence spectrometer with an excitation wavelength of 452 nm. The quenching experiments were performed by the addition of various concentrations of catalysts or BIH to 8 mL of MeCN with a fixed concentration of Ru(bpy)$_3Cl_2$ (0.05 mM). In addition, in the quenching experiment of Ru(bpy)$_3Cl_2$ (0.05 mM) with different catalysts, the concentration of each catalyst was determined to be 0.02 mg/mL.

The quenching rate constant (k_q) was calculated by the Stern−Volmer equation

$$I_0/I = 1 + k_q\tau_0[Q]$$

https://doi.org/10.1021/acscatal.3c01003
ACS Catal. 2023, 13, 8760−8769

where I_0 and I are the emission intensities of the photosensitizer $Ru(bpy)_3Cl_2$ in the absence and presence of quencher Q, respectively, k_q is the bimolecular quenching rate constant, and τ_0 represents the emission lifetime of the excited state without quencher Q. $[Q]$ represents the concentration of the quencher.

4.2.6. In Situ DRIFTS. In situ DRIFTS spectra were collected on a Nicolet iST 10 Fourier transform infrared spectrometer with a mercury cadmium telluride detector, and two CaF_2 were used as windows. In brief, the samples consisting of $Ru(bpy)_3Cl_2$ and the catalyst were packed in a sample cup and sealed in the infrared (IR) reaction chamber under Ar flow. The temperature was set at 120 °C first and maintained for 30 min to remove the residual organic molecules and water. After the temperature was decreased to room temperature, a spectrum of the sample was recorded as the background under Ar. Next, Ar was cut off, and ultra-pure CO_2 (99.999%) after passing through the H_2O trap was introduced for 30 min in the dark. To avoid unnecessary interference under visible light irradiation, the in situ DRIFTS data were analyzed by subtracting the signal at 0 min under light.

4.2.7. Theoretical Calculations. All quantum chemical calculations were carried out based on the ORCA5.0.3 software package.[59−61] The B3LYP hybrid functional[62] combined with DFT-D dispersion correction[63] and def2-TZVP(-f) calculation basis[64] using RIJCOSX[65] were used for geometric optimization and frequency analysis to ensure the stability of the optimized structures. The structures in this work were all local minimum points on the potential energy surface without imaginary frequency. The single-point energy was calculated by the wB97M-V hybrid functional[66] combined with the def2-TZVP calculation basis. The free energy correction was carried out based on the frequency calculation results.

■ ASSOCIATED CONTENT

Supporting Information

The Supporting Information is available free of charge at https://pubs.acs.org/doi/10.1021/acscatal.3c01003.

Materials and instrumentation; material characterizations; and catalytic results (PDF)

■ AUTHOR INFORMATION

Corresponding Author

Hai-Long Jiang − *Department of Chemistry, University of Science and Technology of China, Hefei, Anhui 230026, P. R. China;* orcid.org/0000-0002-2975-7977; Email: jianglab@ustc.edu.cn

Authors

Jingxue Wang − *Department of Chemistry, University of Science and Technology of China, Hefei, Anhui 230026, P. R. China*

Kang Sun − *Department of Chemistry, University of Science and Technology of China, Hefei, Anhui 230026, P. R. China*

Denan Wang − *Department of Chemistry, Marquette University, Milwaukee, Wisconsin 53201, United States;* orcid.org/0000-0003-3603-6788

Xinwei Niu − *School of Energy and Power Engineering, North China Electric Power University, Baoding 071003, P. R. China*

Zhongyuan Lin − *Department of Chemistry, University of Science and Technology of China, Hefei, Anhui 230026, P. R. China*

Siyuan Wang − *Department of Chemistry, University of Science and Technology of China, Hefei, Anhui 230026, P. R. China*

Weijie Yang − *School of Energy and Power Engineering, North China Electric Power University, Baoding 071003, P. R. China;* orcid.org/0000-0002-0232-1129

Jier Huang − *Department of Chemistry, Marquette University, Milwaukee, Wisconsin 53201, United States; Department of Chemistry and Schiller Institute of Integrated Science and Society, Boston College, Chestnut Hill, Massachusetts 02467, United States;* orcid.org/0000-0002-2885-5786

Complete contact information is available at: https://pubs.acs.org/10.1021/acscatal.3c01003

Author Contributions

J.W. and K.S. contributed equally to this work. The manuscript was written through the contributions of all authors. All authors have given approval for the final version of the manuscript.

Notes

The authors declare no competing financial interest.

■ ACKNOWLEDGMENTS

This work was supported by the National Key Research and Development Program of China (2021YFA1500402), the Strategic Priority Research Program of the Chinese Academy of Sciences (XDB0450302), the National Natural Science Foundation of China (U22A20401 and 22161142001), and the International Partnership Program of CAS (123GJHZ2022028MI). The use of the Advanced Photon Source in Argonne National Laboratory was supported by the U. S. Department of Energy, Office of Science, Office of Basic Energy Sciences, under award no. DE-AC02-06CH11357.

■ REFERENCES

(1) Davis, S. J.; Caldeira, K.; Matthews, H. D. Future CO_2 Emissions and Climate Change from Existing Energy Infrastructure. *Science* **2010**, *329*, 1330−1333.

(2) Li, X.; Yu, J.; Jaroniec, M.; Chen, X. Cocatalysts for Selective Photoreduction of CO_2 into Solar Fuels. *Chem. Rev.* **2019**, *119*, 3962−4179.

(3) Feng, C.; Wu, Z.-P.; Huang, K.-W.; Ye, J.; Zhang, H. Surface Modification of 2D Photocatalysts for Solar Energy Conversion. *Adv. Mater.* **2022**, *34*, No. e2200180.

(4) Wang, Y.; Chen, E.; Tang, J. Insight on Reaction Pathways of Photocatalytic CO_2 Conversion. *ACS Catal.* **2022**, *12*, 7300−7316.

(5) Gong, E.; Ali, S.; Hiragond, C. B.; Kim, H. S.; Powar, N. S.; Kim, D.; Kim, H.; In, S. I. Solar fuels: research and development strategies to accelerate photocatalytic CO_2 conversion into hydrocarbon fuels. *Energy Environ. Sci.* **2022**, *15*, 880−937.

(6) Jiao, L.; Wang, J.; Jiang, H.-L. Microenvironment Modulation in Metal-Organic Framework-Based Catalysis. *Acc. Mater. Res.* **2021**, *2*, 327−339.

(7) Wagner, A.; Sahm, C. D.; Reisner, E. Towards molecular understanding of local chemical environment effects in electro- and photocatalytic CO_2 reduction. *Nat. Catal.* **2020**, *3*, 775−786.

(8) Takeda, H.; Cometto, C.; Ishitani, O.; Robert, M. Electrons, Photons, Protons and Earth-Abundant Metal Complexes for Molecular Catalysis of CO_2 Reduction. *ACS Catal.* **2017**, *7*, 70−88.

(9) Xie, W.; Li, K.; Liu, X.-H.; Zhang, X.; Huang, H. P-Mediated Cu-N_4 Sites in Carbon Nitride Realizing CO_2 Photoreduction to C_2H_4 with Selectivity Modulation. *Adv. Mater.* **2023**, *35*, 2208132.
(10) Wang, G.; He, C.-T.; Huang, R.; Mao, J.; Wang, D.; Li, Y. Photoinduction of Cu Single Atoms Decorated on UiO-66-NH_2 for Enhanced Photocatalytic Reduction of CO_2 to Liquid Fuels. *J. Am. Chem. Soc.* **2020**, *142*, 19339−19345.
(11) Wang, J.; Kim, E.; Kumar, D. P.; Rangappa, A. P.; Kim, Y.; Zhang, Y.; Kim, T. Highly Durable and Fully Dispersed Cobalt Diatomic Site Catalysts for CO_2 Photoreduction to CH_4. *Angew. Chem., Int. Ed.* **2022**, *61*, No. e202113044.
(12) Gong, Y.-N.; Shao, B.-Z.; Mei, J.-H.; Yang, W.; Zhong, D.-C.; Lu, T.-B. Facile synthesis of C_3N_4-supported metal catalysts for efficient CO_2 photoreduction. *Nano Res.* **2022**, *15*, 551−556.
(13) Wang, G.; Chen, Z.; Wang, T.; Wang, D.; Mao, J. P and Cu Dual Sites on Graphitic Carbon Nitride for Photocatalytic CO_2 Reduction to Hydrocarbon Fuels with High C_2H_6 Evolution. *Angew. Chem., Int. Ed.* **2022**, *61*, No. e202210789.
(14) Wang, Y.; Qu, Y.; Qu, B.; Bai, L.; Liu, Y.; Yang, Z.-D.; Zhang, W.; Jing, L.; Fu, H. Construction of Six-Oxygen-Coordinated Single Ni Sites on g-C_3N_4 with Boron-Oxo Species for Photocatalytic Water-Activation-Induced CO_2 Reduction. *Adv. Mater.* **2021**, *33*, 2105482.
(15) Zhang, H.; Wei, J.; Dong, J.; Liu, G.; Shi, L.; An, P.; Zhao, G.; Kong, J.; Wang, X.; Meng, X.; Zhang, J.; Ye, J. Efficient Visible-Light-Driven Carbon Dioxide Reduction by a Single-Atom Implanted Metal-Organic Framework. *Angew. Chem., Int. Ed.* **2016**, *55*, 14310−14314.
(16) Fang, Z.-B.; Liu, T.-T.; Liu, J.; Jin, S.; Wu, X.-P.; Gong, X.-Q.; Wang, K.; Yin, Q.; Liu, T.-F.; Cao, R.; Zhou, H.-C. Boosting Interfacial Charge-Transfer Kinetics for Efficient Overall CO_2 Photoreduction via Rational Design of Coordination Spheres on Metal-Organic Frameworks. *J. Am. Chem. Soc.* **2020**, *142*, 12515−12523.
(17) Xia, B.; Yang, Y.; Zhang, Y.; Xia, Y.; Jaroniec, M.; Yu, J.; Ran, J.; Qiao, S.-Z. Metal−organic framework with atomically dispersed Ni-N_4 sites for greatly-raised visible-light photocatalytic H_2 production. *Chem. Eng. J.* **2022**, *431*, 133944.
(18) Furukawa, H.; Cordova, K. E.; O'Keeffe, M.; Yaghi, O. M. The Chemistry and Applications of Metal-Organic Frameworks. *Science* **2013**, *341*, 1230444.
(19) Zhao, X.; Wang, Y.; Li, D.-S.; Bu, X.; Feng, P. Metal-Organic Frameworks for Separation. *Adv. Mater.* **2018**, *30*, 1705189.
(20) Li, H.; Li, L.; Lin, R.-B.; Zhou, W.; Zhang, Z.; Xiang, S.; Chen, B. Porous metal-organic frameworks for gas storage and separation: Status and challenges. *EnergyChem* **2019**, *1*, 100006.
(21) Jiao, L.; Wang, Y.; Jiang, H.-L.; Xu, Q. Metal-Organic Frameworks as Platforms for Catalytic Applications. *Adv. Mater.* **2018**, *30*, 1703663.
(22) Guo, J.; Qin, Y.; Zhu, Y.; Zhang, X.; Long, C.; Zhao, M.; Tang, Z. Metal-organic frameworks as catalytic selectivity regulators for organic transformations. *Chem. Soc. Rev.* **2021**, *50*, 5366−5396.
(23) Pattengale, B.; SantaLucia, D. J.; Yang, S.; Hu, W.; Liu, C.; Zhang, X.; Berry, J. F.; Huang, J. Direct Observation of Node-to-Node Communication in Zeolitic Imidazolate Frameworks. *J. Am. Chem. Soc.* **2018**, *140*, 11573−11576.
(24) Zhao, C.; Jiang, Z.; Liu, Y.; Zhou, Y.; Yin, P.; Ke, Y.; Deng, H. Molecular Compartments Created in Metal-Organic Frameworks for Efficient Visible-Light-Driven CO_2 Overall Conversion. *J. Am. Chem. Soc.* **2022**, *144*, 23560−23571.
(25) Wei, Y.-S.; Zhang, M.; Zou, R.; Xu, Q. Metal-Organic Framework-Based Catalysts with Single Metal Sites. *Chem. Rev.* **2020**, *120*, 12089−12174.
(26) Dhakshinamoorthy, A.; Li, Z.; Garcia, H. Catalysis and photocatalysis by metal organic frameworks. *Chem. Soc. Rev.* **2018**, *47*, 8134−8172.
(27) Liu, J.; Goetjen, T. A.; Wang, Q.; Knapp, J. G.; Wasson, M. C.; Yang, Y.; Syed, Z. H.; Delferro, M.; Notestein, J. M.; Farha, O. K.; Hupp, J. T. MOF-enabled confinement and related effects for chemical catalyst presentation and utilization. *Chem. Soc. Rev.* **2022**, *51*, 1045−1097.
(28) Cui, W.-G.; Zhang, G.-Y.; Hu, T.-L.; Bu, X.-H. Metal-organic framework-based heterogeneous catalysts for the conversion of C1 chemistry: CO, CO_2 and CH_4. *Coord. Chem. Rev.* **2019**, *387*, 79−120.
(29) Sun, K.; Qian, Y.; Jiang, H.-L. Metal-Organic Frameworks for Photocatalytic Water Splitting and CO_2 Reduction. *Angew. Chem., Int. Ed.* **2023**, *62*, No. e202217565.
(30) Lan, G.; Fan, Y.; Shi, W.; You, E.; Veroneau, S. S.; Lin, W. Biomimetic active sites on monolayered metal-organic frameworks for artificial photosynthesis. *Nat. Catal.* **2022**, *5*, 1006−1018.
(31) Guo, F.; Yang, M.; Li, R.-X.; He, Z.-Z.; Wang, Y.; Sun, W.-Y. Nanosheet-Engineered NH_2-MIL-125 with Highly Active Facets for Enhanced Solar CO_2 Reduction. *ACS Catal.* **2022**, *12*, 9486−9493.
(32) Li, J.; Huang, H.; Xue, W.; Sun, K.; Song, X.; Wu, C.; Nie, L.; Li, Y.; Liu, C.; Pan, Y.; Jiang, H.-L.; Mei, D.; Zhong, C. Self-adaptive dual-metal-site pairs in metal-organic frameworks for selective CO_2 photoreduction to CH_4. *Nat. Catal.* **2021**, *4*, 719−729.
(33) Huang, N.-Y.; He, H.; Liu, S.; Zhu, H.-L.; Li, Y.-J.; Xu, J.; Huang, J.-R.; Wang, X.; Liao, P.-Q.; Chen, X.-M. Electrostatic Attraction-Driven Assembly of a Metal-Organic Framework with a Photosensitizer Boosts Photocatalytic CO_2 Reduction to CO. *J. Am. Chem. Soc.* **2021**, *143*, 17424−17430.
(34) Fu, Y.; Sun, D.; Chen, Y.; Huang, R.; Ding, Z.; Fu, X.; Li, Z. An Amine-Functionalized Titanium Metal-Organic Framework Photocatalyst with Visible-Light-Induced Activity for CO_2 Reduction. *Angew. Chem., Int. Ed.* **2012**, *51*, 3364−3367.
(35) Yu, F.; Jing, X.; Wang, Y.; Sun, M.; Duan, C. Hierarchically Porous Metal-Organic Framework/MoS_2 Interface for Selective Photocatalytic Conversion of CO_2 with H_2O into CH_3COOH. *Angew. Chem., Int. Ed.* **2021**, *60*, 24849−24853.
(36) Xia, Y.-S.; Tang, M.; Zhang, L.; Liu, J.; Jiang, C.; Gao, G.-K.; Dong, L.-Z.; Xie, L.-G.; Lan, Y.-Q. Tandem utilization of CO_2 photoreduction products for the carbonylation of aryl iodides. *Nat. Commun.* **2022**, *13*, 2964.
(37) Islamoglu, T.; Goswami, S.; Li, Z.; Howarth, A. J.; Farha, O. K.; Hupp, J. T. Postsynthetic Tuning of Metal-Organic Frameworks for Targeted Applications. *Acc. Chem. Res.* **2017**, *50*, 805−813.
(38) Yang, S.; Pattengale, B.; Lee, S.; Huang, J. Real-Time Visualization of Active Species in a Single-Site Metal-Organic Framework Photocatalyst. *ACS Energy Lett.* **2018**, *3*, 532−539.
(39) Huang, N.-Y.; Shen, J.-Q.; Zhang, X.-W.; Liao, P.-Q.; Zhang, J.-P.; Chen, X.-M. Coupling Ruthenium Bipyridyl and Cobalt Imidazolate Units in a Metal-Organic Framework for an Efficient Photosynthetic Overall Reaction in Diluted CO_2. *J. Am. Chem. Soc.* **2022**, *144*, 8676−8682.
(40) Karmakar, S.; Barman, S.; Rahimi, F. A.; Maji, T. K. Covalent grafting of molecular photosensitizer and catalyst on MOF-808: effect of pore confinement toward visible light-driven CO_2 reduction in water. *Energy Environ. Sci.* **2021**, *14*, 2429−2440.
(41) Choi, K. M.; Kim, D.; Rungtaweevoranit, B.; Trickett, C. A.; Barmanbek, J. T. D.; Alshammari, A. S.; Yang, P.; Yaghi, O. M. Plasmon-Enhanced Photocatalytic CO_2 Conversion within Metal-Organic Frameworks under Visible Light. *J. Am. Chem. Soc.* **2017**, *139*, 356−362.
(42) Liao, W.-M.; Zhang, J.-H.; Wang, Z.; Yin, S.-Y.; Pan, M.; Wang, H.-P.; Su, C.-Y. Post-synthetic exchange (PSE) of UiO-67 frameworks with Ru/Rh half-sandwich units for visible-light-driven H_2 evolution and CO_2 reduction. *J. Mater. Chem. A* **2018**, *6*, 11337−11345.
(43) Zhuo, T.-C.; Song, Y.; Zhuang, G.-L.; Chang, L.-P.; Yao, S.; Zhang, W.; Wang, Y.; Wang, P.; Lin, W.; Lu, T.-B.; Zhang, Z.-M. H-Bond-Mediated Selectivity Control of Formate versus CO during CO_2 Photoreduction with Two Cooperative Cu/X Sites. *J. Am. Chem. Soc.* **2021**, *143*, 6114−6122.
(44) Chen, C.; Wu, T.; Wu, H.; Liu, H.; Qian, Q.; Liu, Z.; Yang, G.; Han, B. Highly effective photoreduction of CO_2 to CO promoted by integration of CdS with molecular redox catalysts through metal-organic frameworks. *Chem. Sci.* **2018**, *9*, 8890−8894.

https://doi.org/10.1021/acscatal.3c01003
ACS Catal. 2023, 13, 8760−8769

(45) Hendon, C. H.; Bonnefoy, J.; Quadrelli, E. A.; Canivet, J.; Chambers, M. B.; Rousse, G.; Walsh, A.; Fontecave, M.; Mellot-Draznieks, C. A Simple and Non-Destructive Method for Assessing the Incorporation of Bipyridine Dicarboxylates as Linkers within Metal-Organic Frameworks. *Chem.—Eur. J.* **2016**, *22*, 3713−3718.
(46) Gong, Y.-N.; Zhong, W.; Li, Y.; Qiu, Y.; Zheng, L.; Jiang, J.; Jiang, H.-L. Regulating Photocatalysis by Spin-State Manipulation of Cobalt in Covalent Organic Frameworks. *J. Am. Chem. Soc.* **2020**, *142*, 16723−16731.
(47) Zhou, Y.; Hu, W.; Yang, S.; Zhang, Y.; Nyakuchena, J.; Duisenova, K.; Lee, S.; Fan, D.; Huang, J. Site-Selective Probes of Mixed-Node Metal Organic Frameworks for Photocatalytic Hydrogen Generation. *J. Phys. Chem. C* **2020**, *124*, 1405−1412.
(48) Hu, W.; Wang, D.; Ma, Q.; Reinhart, B. J.; Zhang, X.; Huang, J. The Impact of Axial Ligation on the Excited State Dynamics of Cobalt(II) Phthalocyanine. *J. Photoch. Photobiol.* **2022**, *11*, 100132.
(49) Puntoriero, F.; Serroni, S.; La Ganga, G.; Santoro, A.; Galletta, M.; Nastasi, F.; La Mazza, E.; Cancelliere, A. M.; Campagna, S. Photo- and Redox-Active Metal Dendrimers: A Journey from Molecular Design to Applications and Self-Aggregated Systems. *Eur. J. Inorg. Chem.* **2018**, 3887−3899.
(50) Prier, C. K.; Rankic, D. A.; MacMillan, D. W. C. Visible Light Photoredox Catalysis with Transition Metal Complexes: Applications in Organic Synthesis. *Chem. Rev.* **2013**, *113*, 5322−5363.
(51) Bock, C. R.; Connor, J. A.; Gutierrez, A. R.; Meyer, T. J.; Whitten, D. G.; Sullivan, B. P.; Nagle, J. K. Estimation of excited-state redox potentials by electron-transfer quenching. Application of electron-transfer theory to excited-state redox processes. *J. Am. Chem. Soc.* **1979**, *101*, 4815−4824.
(52) Li, N.; Wang, B.; Si, Y.; Xue, F.; Zhou, J.; Lu, Y.; Liu, M. Toward High-Value Hydrocarbon Generation by Photocatalytic Reduction of CO_2 in Water Vapor. *ACS Catal.* **2019**, *9*, 5590−5602.
(53) Khrizanforov, M.; Strekalova, S.; Khrizanforova, V.; Dobrynin, A.; Kholin, K.; Gryaznova, T.; Grinenko, V.; Gubaidullin, A.; Kadirov, M. K.; Budnikova, Y. Cobalt-Catalyzed Green Cross-Dehydrogenative C(sp^2)-H/P-H Coupling Reactions. *Top. Catal.* **2018**, *61*, 1949−1956.
(54) Lee, I.-S. H.; Jeoung, E. H.; Kreevoy, M. M. Marcus Theory of a Parallel Effect on α for Hydride Transfer Reaction between NAD^+ Analogues. *J. Am. Chem. Soc.* **1997**, *119*, 2722−2728.
(55) SantaLucia, D. J.; Hu, W.; Wang, D.; Huang, J.; Berry, J. F. Postsynthetic Treatment of ZIF-67 with 5-Methyltetrazole: Evolution from Pseudo-T_d to Pseudo-O_h Symmetry and Collapse of Magnetic Ordering. *Inorg. Chem.* **2022**, *61*, 6056−6062.
(56) Zhang, Y.; Hu, W.; Wang, D.; Reinhart, B. J.; Huang, J. Electron shuttle in the MOF derived TiO_2/CuO heterojunction boosts light driven hydrogen evolution. *J. Mater. Chem. A* **2021**, *9*, 6180−6187.
(57) Connelly, N. G.; Geiger, W. E. Chemical Redox Agents for Organometallic Chemistry. *Chem. Rev.* **1996**, *96*, 877−910.
(58) Liu, H.; Xu, C.; Li, D.; Jiang, H.-L. Photocatalytic Hydrogen Production Coupled with Selective Benzylamine Oxidation over MOF Composites. *Angew. Chem., Int. Ed.* **2018**, *57*, 5379−5383.
(59) Neese, F. The ORCA program system. *WIREs Comput. Mol. Sci.* **2011**, *2*, 73−78.
(60) Neese, F. Software update: The ORCA program system—Version 5.0. *Wiley Interdiscip. Rev.: Comput. Mol. Sci.* **2022**, *12*, No. e1606.
(61) Neese, F.; Wennmohs, F.; Becker, U.; Riplinger, C. The ORCA quantum chemistry program package. *J. Chem. Phys.* **2020**, *152*, 224108.
(62) Stephens, P. J.; Devlin, F. J.; Chabalowski, C. F.; Frisch, M. J. Ab Initio Calculation of Vibrational Absorption and Circular Dichroism Spectra Using Density Functional Force Fields. *J. Phys. Chem.* **1994**, *98*, 11623−11627.
(63) Grimme, S.; Antony, J.; Ehrlich, S.; Krieg, H. A consistent and accurate ab initio parametrization of density functional dispersion correction (DFT-D) for the 94 elements H-Pu. *J. Chem. Phys.* **2010**, *132*, 154104.
(64) Weigend, F.; Ahlrichs, R. Balanced basis sets of split valence, triple zeta valence and quadruple zeta valence quality for H to Rn: Design and assessment of accuracy. *Phys. Chem. Chem. Phys.* **2005**, *7*, 3297−3305.
(65) Neese, F.; Wennmohs, F.; Hansen, A.; Becker, U. Efficient, approximate and parallel Hartree−Fock and hybrid DFT calculations. A 'chain-of-spheres' algorithm for the Hartree−Fock exchange. *Chem. Phys.* **2009**, *356*, 98−109.
(66) Mardirossian, N.; Head-Gordon, M. ωB97M-V: A combinatorially optimized, range-separated hybrid, meta-GGA density functional with VV10 nonlocal correlation. *J. Chem. Phys.* **2016**, *144*, 214110.

Recommended by ACS

Regulating the N Coordination Environment of Co Single-Atom Nanozymes for Highly Efficient Oxidase Mimics
Zhe Li, Yizhong Lu, *et al.*
FEBRUARY 03, 2023
NANO LETTERS
READ

Oxygen Reduction Reaction Activity in Non-Precious Single-Atom (M–N/C) Catalysts—Contribution of Metal and Carbon/Nitrogen Framework-Based Sites
Mengjun Gong, Anthony Kucernak, *et al.*
MAY 01, 2023
ACS CATALYSIS
READ

Atomically Dispersed Metal–Nitrogen–Carbon Catalysts with *d*-Orbital Electronic Configuration-Dependent Selectivity for Electrochemical CO_2-to-CO Reduction
Jialin Wang, Shaohua Shen, *et al.*
FEBRUARY 01, 2023
ACS CATALYSIS
READ

Competition of CO and Acetaldehyde Adsorption and Reduction on Copper Electrodes and Its Impact on *n*-Propanol Formation
Alisson H. M. da Silva, Marc T. M. Koper, *et al.*
MARCH 15, 2023
ACS CATALYSIS
READ

Get More Suggestions >

https://doi.org/10.1021/acscatal.3c01003
ACS Catal. 2023, 13, 8760−8769